Spectral Observations and Modeling of a Solar White-light Flare Observed by CHASE

De-Chao Song[1,2] , Jun Tian[1,2] , Y. Li[1,2] , M. D. Ding[3,4] , Yang Su[1,2] , Sijie Yu[5] , Jie Hong[3,4] , Ye Qiu[3,4] ,
Shihao Rao[3,4] , Xiaofeng Liu[1,2] , Qiao Li[1,2] , Xingyao Chen[6] , Chuan Li[3,4] , and Cheng Fang[3,4]

[1] Key Laboratory of Dark Matter and Space Astronomy, Purple Mountain Observatory, CAS, Nanjing 210023, People's Republic of China; yingli@pmo.ac.cn
[2] School of Astronomy and Space Science, University of Science and Technology of China, Hefei 230026, People's Republic of China
[3] School of Astronomy and Space Science, Nanjing University, Nanjing 210023, People's Republic of China; dmd@nju.edu.cn
[4] Key Laboratory for Modern Astronomy and Astrophysics (Nanjing University), Ministry of Education, Nanjing 210023, People's Republic of China
[5] Center for Solar-Terrestrial Research, New Jersey Institute of Technology, 323 Martin Luther King Jr. Blvd., Newark, NJ 07102-1982, USA
[6] School of Physics & Astronomy, University of Glasgow, Glasgow G12 8QQ, UK
Received 2023 May 5; revised 2023 June 20; accepted 2023 June 26; published 2023 July 20

Abstract

The heating mechanisms of solar white-light flares remain unclear. We present an X1.0 white-light flare on 2022 October 2 (SOL2022-10-02T20:25) observed by the Chinese Hα Solar Explorer that provides two-dimensional spectra in the visible light for the full solar disk with a seeing-free condition. The flare shows a prominent enhancement of ∼40% in the photospheric Fe I line at 6569.2 Å, and the nearby continuum also exhibits a maximum enhancement of ∼40%. For the continuum near the Fe I line at 6173 Å from the Helioseismic and Magnetic Imager on board the Solar Dynamics Observatory, it is enhanced up to ∼20%. At the white-light kernels, the Fe I line at 6569.2 Å has a symmetric Gaussian profile that is still in absorption and the Hα line at 6562.8 Å displays a very broad emission profile with a central reversal plus a red or blue asymmetry. The white-light kernels are cospatial with the microwave footpoint sources observed by the Expanded Owens Valley Solar Array and the time profile of the white-light emission matches that of the hard X-ray emission above 30 keV from the Gamma-ray Burst Monitor (GBM) on Fermi. These facts indicate that the white-light emission is qualitatively related to a nonthermal electron beam. We also perform a radiative hydrodynamic simulation with the electron-beam parameters constrained by the hard X-ray observations from Fermi/GBM. The result reveals that the white-light enhancement cannot be well explained by a pure electron-beam heating together with its induced radiative backwarming but may need additional heating sources such as Alfvén waves.

Unified Astronomy Thesaurus concepts: Solar activity (1475); Solar flares (1496); Solar flare spectra (1982); Solar photosphere (1518); Solar chromosphere (1479); Solar x-ray emission (1536)

1. Introduction

White-light flares (WLFs) belong to a relatively rare type of flares characterized by a sudden increase in the visible continuum. The first solar flare ever observed, the so-called Carrington event (Carrington 1859), was a typical WLF. WLFs have also been observed on other stars (e.g., Pugh et al. 2016). Solar WLFs can be divided into two types (e.g., Machado et al. 1986). Type I WLFs have a well-established correlation between the peak time of continuum emission and that of hard X-ray (HXR) and microwave emissions, which also show an evident Balmer jump in the continuous spectrum (e.g., Fang & Ding 1995). By contrast, type II WLFs lack those features (e.g., Ding et al. 1999; Procházka et al. 2018). It should be noted that some WLFs show observational characteristics in between these two types, highlighting a complexity of the heating mechanisms underlying WLFs (e.g., Hiei 1982; Hao et al. 2017).

In recent decades, various heating mechanisms have been proposed for WLFs based on observations and simulations, including nonthermal electron-beam bombardment (e.g., Hudson et al. 1992; Krucker et al. 2015; Watanabe & Imada 2020), proton beam bombardment (e.g., Machado et al. 1978; Henoux et al. 1993; Procházka 2019), radiative backwarming (e.g., Metcalf et al. 1990; Ding et al. 2003; Song et al. 2018),

chromospheric condensation (e.g., Gan et al. 1992; Kowalski et al. 2015), Alfvén wave dissipation (e.g., Emslie & Sturrock 1982; Fletcher & Hudson 2008), and soft X-ray (SXR)/EUV irradiation (e.g., Henoux & Nakagawa 1977; Poland et al. 1988). Nevertheless, the heating mechanisms of WLFs have not been fully understood. In some events, it is likely that the enhancement of white-light emission is caused by a joint effect of multiple mechanisms as mentioned above (e.g., Machado et al. 1978; Xu et al. 2010).

Besides the continuum, spectral lines like the Fe I and Hα lines have been used to diagnose the heating mechanisms of WLFs (e.g., Lin et al. 1996; Baranovsky & Kurochka 1997; Yang et al. 2021; Hong et al. 2022). Babin & Koval 1992 reported that in an X12 WLF, several Fe I lines in the wavelength range of 6517–6598 Å lack an absorption in the profiles. Jurčák et al. (2018) observed emission profiles in the Fe I λ6301 and λ6302 lines in an X9.3 WLF and judged that the continuum enhancement mainly originates from the heated chromosphere rather than the photosphere. In an M2.0 flare, the Fe I λ6173 line was found to remain in absorption and become blueshifted (Martínez Oliveros et al. 2011). Based on radiative hydrodynamic simulations in a flaring atmosphere, Hong et al. (2018) found that the enhancement of the Fe I λ6173 line can be caused by both electron-beam heating in the lower chromosphere and radiative backwarming in the photosphere. Regarding the Hα λ6563 line, it is much more complicated. For example, it can be double-peaked with usually a red asymmetry in WLFs (Babin & Koval 1992; Zhou et al. 1997).

In this Letter, we present an X1.0 WLF on 2022 October 2 well observed by the Chinese Hα Solar Explorer (CHASE; Li et al. 2019, 2022), which provides spectral observations in the Fe I λ6569 and Hα lines simultaneously with a seeing-free condition. This is the first X-class flare captured by CHASE. It shows a prominent enhancement of ∼40% in the Fe I line and the nearby continuum can also be enhanced up to 40%. The white-light brightenings are related to HXR and microwave emissions spatially or temporally. A radiative hydrodynamic simulation with the parameters constrained by HXR observations reveals that such a prominent enhancement cannot be explained by a pure electron-beam heating together with its induced radiative backwarming but needs additional heating sources.

2. Observations and Data Reduction

The X1.0 flare under study was observed by multiple space- and ground-based telescopes. CHASE captured the main phase of the flare and acquired the two-dimensional spectra of Fe I λ6569 (6567.5–6569.8 Å) and Hα λ6563 (6559.4–6565.2 Å) simultaneously for the full disk via a raster scanning mode. The spatial, temporal, and spectral resolutions of CHASE imaging spectral data in a two-binning mode here are ∼1″ pixel⁻¹, ∼1 minute, and 0.05 Å pixel⁻¹, respectively. The data have been processed with corrections for dark field, flat field, and slit image curvature, as well as wavelength calibration (Qiu et al. 2022). When measuring the relative enhancements of the continuum, Fe I line, and Hα line intensities, we calculate the standard deviation of intensities in difference images for a relatively quiet region as their uncertainties. The Fe I and Hα lines are analyzed by adopting a single Gaussian fitting and a bisector method, respectively. In order to quantitatively measure the Doppler velocity, we need an accurate reference wavelength that is obtained by averaging the line profiles over the quiet region. This yields velocity uncertainties of ∼1 and ∼4 km s⁻¹ for the Fe I and Hα lines, respectively. The Helioseismic and Magnetic Imager (HMI; Scherrer et al. 2012) on board the Solar Dynamics Observatory (SDO; Pesnell et al. 2012) provides the pseudo-continuum images at Fe I λ6173 with a cadence of 45 s for the entire flare phase. We also measure the relative enhancement of this continuum. The Atmospheric Imaging Assembly (AIA; Lemen et al. 2012) on SDO provides the EUV images at 131 Å, in which the hot flare loops are clearly visible. The Gamma-ray Burst Monitor (GBM; Meegan et al. 2009) on Fermi provides HXR data in the energy range from 8 keV to 40 MeV. We select the data from detector N4 to invert the nonthermal electron-beam parameters assuming a thick-target model (Brown 1971). The Expanded Owens Valley Solar Array (EOVSA; Gary et al. 2018) provides microwave spectral imaging observations at 1–18 GHz. The X-Ray Sensor (XRS; Hanser & Sellers 1996) on Geostationary Operational Environmental Satellite (GOES) provides the SXR emission at 1–8 Å.

3. Results

3.1. Overview of the X1.0 White-light Flare

The X1.0 flare started at 19:53 UT and peaked at 20:25 UT on 2022 October 2. From Figure 1(a) one can see that the Fermi HXR emission above 30 keV peaks at nearly the same time (∼20:22 UT) as the time derivative of SXR flux, i.e., implying the validity of Neupert effect (Neupert 1968). From Figure 1(b)

it is seen that the HMI continuum, CHASE continuum, and Fe I and Hα line intensities (integrated over the flaring region as shown in Figures 1(c)–(g)) also peak at ∼20:22 UT. Moreover, the former three appear to match the HXR emission or the time derivative of SXR flux temporally. From the CHASE (or HMI) continuum and Fe I images (Figures 1(c)–(f)) we identify multiple white-light brightening kernels, denoted as K1–K3, which lie within the Hα ribbons (see Figure 1(g)). Note that the white-light kernels and Hα ribbons show an outward motion as the flare evolves. Kernel K1 is located outside the sunspot and shows up earlier, while K2 and K3 are in the penumbra with opposite magnetic polarities (see Figure 1(d)) and appear at a later time of ∼20:22 UT. In particular, kernels K2 and K3 seem to be conjugate footpoints of some flare loops as seen in AIA 131 Å image (Figure 1(h)). The EOVSA microwave sources (marked by the contours in Figures 1(d)–(h)) also match the flare loops and their footpoints quite well. It should be mentioned that there presents a nonthermal source at the footpoints as revealed by the microwave spectral fitting. From the HXR and also microwave observations, we can conclude that there is a qualitative relationship between the white-light brightenings and the nonthermal electron-beam heating.

3.2. Spectral Features of the White-light Kernels from CHASE

Figures 2(a)–(c) show the temporal evolution of the relative enhancements of HMI continuum, CHASE continuum, Fe I line, and Hα line for kernels K1–K3 (summed over an area of 3″ × 3″), together with the SXR flux and its time derivative. One can see that for all the kernels, the intensity curves all exhibit a sharp rise followed by a relatively gradual decay. The brightening at K1 peaks about 1 minute before but that at K2 and K3 peaks at nearly the same time as the time derivative of SXR flux. At K1, the maximum enhancements of HMI and CHASE continua are 4.3% and 13%, respectively, and those of Fe I (integrated over ±0.5 Å) and Hα (integrated over ±2.3 Å) lines are 11% and 151%, respectively. For K2 and K3, the maximum enhancements are relatively large and up to 13%, 34%, 32%, and 214% for the four wave bands, respectively.

Figures 2(d)–(f) display the temporal evolution of the Fe I and Hα line profiles for K1–K3 (averaged over an area of 3″ × 3″). It is seen that at K1, the Fe I profile has a symmetric Gaussian shape that remains in absorption during the whole period. The nearby continuum exhibits a notable enhancement at 20:21 UT (see the profile in blue in Figure 2(d)), so does the Fe I line center. It should be mentioned that the blue-wing intensity of the Fe I line rises notably at that time, which does not represent the pure continuum emission but is likely affected by the red-wing emission of the Hα line that is largely broadened. The Fe I profiles and the nearby continuum at K2 and K3 are similar to those at K1. The only difference is that the relative enhancements at K2 and K3 are larger than that at K1. Finally, the Fe I profiles at K1–K3 exhibit a very small Doppler velocity within 2 km s⁻¹ during the flare. For the Hα profiles at K1–K3, they show a significant enhancement in intensity and also a notable change in shape from absorption to emission with, however, a central reversal. The Hα profiles become very broad, whose wings are significantly out of the CHASE spectral window. It is interesting that the Hα profiles exhibit different asymmetries at the three kernels especially when the continuum is significantly enhanced. At K1 and K2, the most enhanced Hα profiles mainly show a red symmetry with the line center slightly blueshifted (Figures 2(d) and (e)).
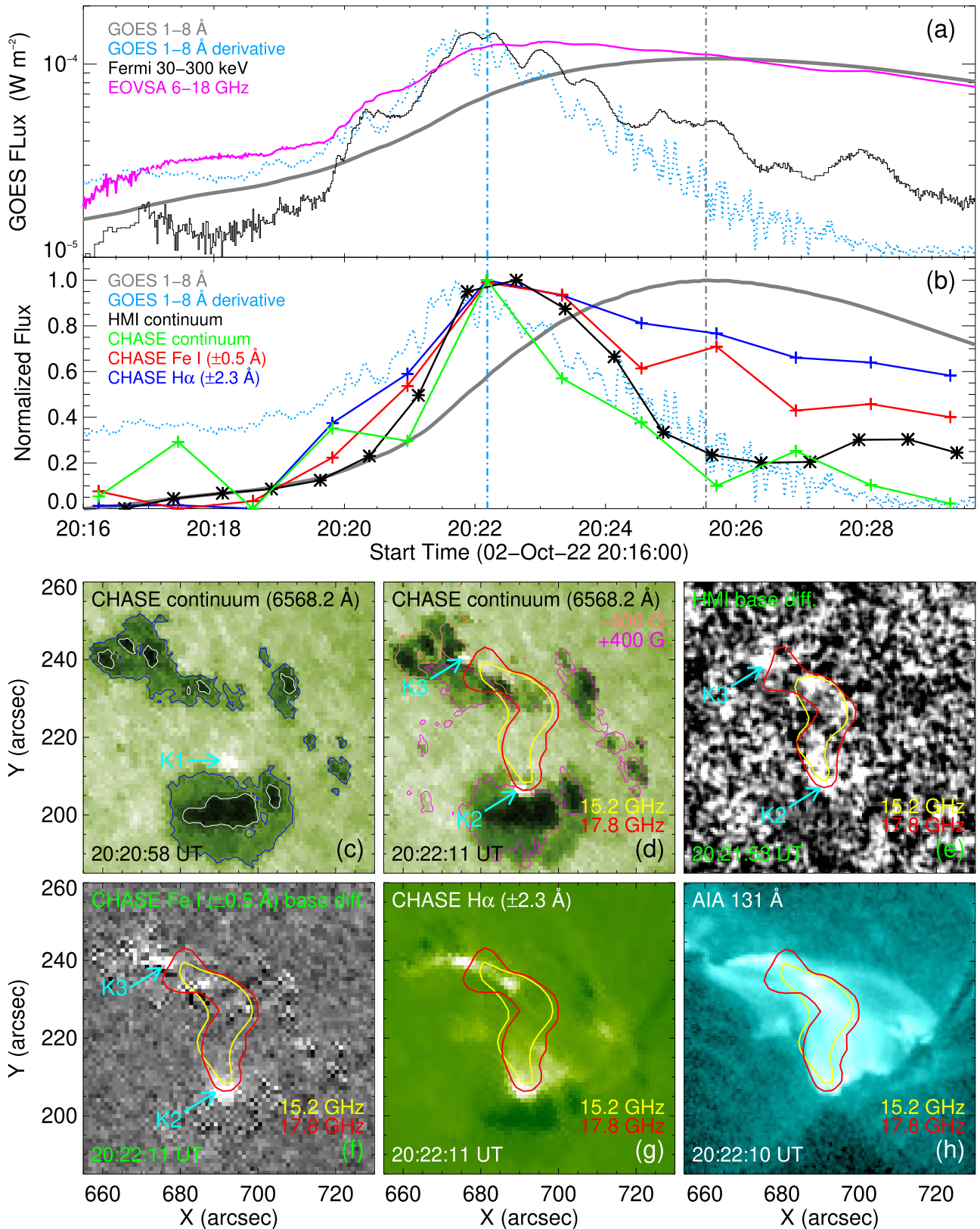
Figure 1. (a) Light curves of GOES SXR 1–8 Å, its time derivative, Fermi HXR 30–300 keV, and EOVSA microwave 6–18 GHz for the flare. (b) HMI continuum (near 6173 Å), CHASE continuum (at 6568.2 Å), Fe I (integrated over ±0.5 Å), and Hα (integrated over ±2.3 Å) intensity curves summed over the field of view of the images as shown in panels (c)–(g), together with the SXR 1–8 Å flux and its time derivative. The gray and blue vertical lines in panels (a) and (b) denote the peak times of the SXR flux and its time derivative, respectively. (c)–(h) CHASE continuum, HMI continuum (base difference), CHASE Fe I (base difference), CHASE Hα, and AIA 131 Å images for the flare. Three white-light brightening kernels (K1–K3) are indicated by three arrows in panels (c)–(f). The white and blue contours in panel (c) mark the sunspot umbra and penumbra, respectively. The magenta and orange contours in panel (d) denote the magnetic polarities at +400 and −400 G, respectively. The yellow and red contours in panels (d)–(h) show the microwave sources at 15.2 and 17.8 GHz, respectively.
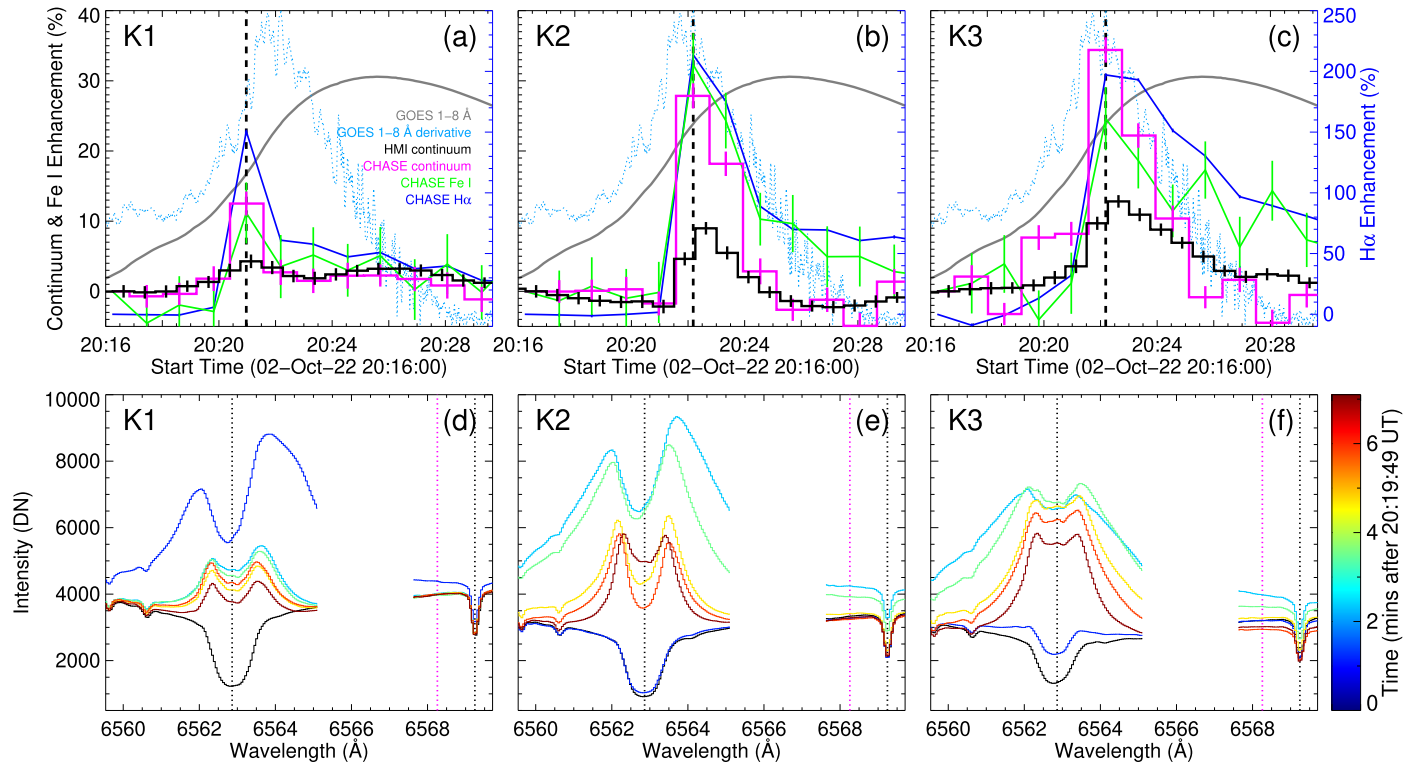
Figure 2. (a)–(c) Temporal evolution of the relative enhancements of HMI continuum, CHASE continuum, Fe I line, and Hα line for kernels K1–K3 summed over an area of $3'' \times 3''$, together with the SXR 1–8 Å flux and its time derivative. The uncertainties of continuum and line intensity enhancements are plotted in error bars. Note that the uncertainty in Hα is quite small compared with its enhancement. The continuum intensity is from the wavelength at 6568.2 Å as indicated by the magenta vertical line in panels (d)–(f) and the Fe I and Hα line intensities are integrated over the wavelengths of ± 0.5 Å and ± 2.3 Å, respectively. The black dashed vertical line denotes the peak time of the three intensity curves from CHASE. (d)–(f) Temporal evolution of the Fe I and Hα line profiles (averaged over an area of $3'' \times 3''$) at K1–K3. The line centers of Fe I and Hα are marked by two black dotted vertical lines in each panel.

However, the most enhanced profile at K3 displays a blue asymmetry or a blue-wing enhancement (Figure 2(f)).

We further make a spectral analysis of the contrast profiles of Fe I and Hα at the peak time for K1–K3, as shown in Figure 3. Note that the profiles here are only from a single pixel for each kernel in order not to lose spectral features due to spatial averaging. The contrast profile is defined as the one with the preflare profile subtracted. From Figures 3(a)–(c) we can see that all the contrast profiles of Fe I are symmetric, which can be well fitted by a single Gaussian function. At K1, the Fe I line center shows an enhancement of 19.0% and the nearby continuum is enhanced with a relatively lower value of 12.4%. The Doppler velocity of the Fe I line at K1 is almost zero. At K2 and K3, the enhancement of Fe I line center can be up to 40.5% and the nearby continuum is enhanced up to 40.2%. Note that the maximum enhancement of Fe I line center and that of the continuum are not cospatial. The contrast profiles of Fe I at K2 and K3 are redshifted with velocities of ~ 1 km s^{-1}. For Hα as shown in Figures 3(d)–(f)), the enhancements at K1–K3 are 185%, 246%, and 222%, respectively. The Hα contrast profiles at K1 and K2 display a notable red asymmetry and the median redshift velocities derived from bisector are 34.4 and 27.7 km s^{-1}, respectively. By comparison, the contrast profile at K3 exhibits a blue-wing enhancement resulting in a blueshift velocity of 16.5 km s^{-1}.

3.3. Radiative Hydrodynamic Simulation and Comparison with Observations

To understand the white-light enhancement of this flare, we perform a radiative hydrodynamic simulation via RADYN

(e.g., Carlsson & Stein 1992, 2002) with an electron-beam heating constrained by the Fermi HXR observations. Since RADYN is a one-dimensional loop model, here we construct 18 sequential flare loops (L1–L18) corresponding to the bumps in the time derivative of SXR flux during 20:19–20:25 UT, i.e., the main phase of the flare (see Figure 4(a)), in a similar way to that in Rubio da Costa et al. (2016). The inputs of each loop including the energy flux, low-energy cutoff, and spectral index of the nonthermal electron beam (as plotted in Figure 4(b) and also listed in Table 1) are obtained from the HXR spectral fitting. Two examples of the spectral fitting are shown in Figures 4(c) and (d) with the time intervals corresponding to the heating episodes of L6 and L11 in principle, respectively. Note that the energy flux is estimated by the total energy divided by the area of Hα sources that are believed to be sensitive to nonthermal electrons (e.g., Fang et al. 1993). Considering that the white-light kernels are located in the region outside the sunspot (RoS; e.g., K1) or in the penumbra (P; K2 and K3), we adopt two different model atmospheres, the quiet-Sun model VAL-C (Vernazza et al. 1981) and the penumbral model (Ding & Fang 1989), as the initial atmospheres. The Hα line is calculated in RADYN under the non-LTE condition at an emergent angle of $\mu = 0.77$, while the Fe I $\lambda 6569$ and $\lambda 6173$ lines are calculated via the radiative transfer code of RH (Uitenbroek 2001; Pereira & Uitenbroek 2015) under the LTE condition (Hong et al. 2022) with $\mu = 0.656$ based on the flare location. The enhancements of the Fe I line center and nearby continuum intensities from simulations are given in Table 1, which can be compared with
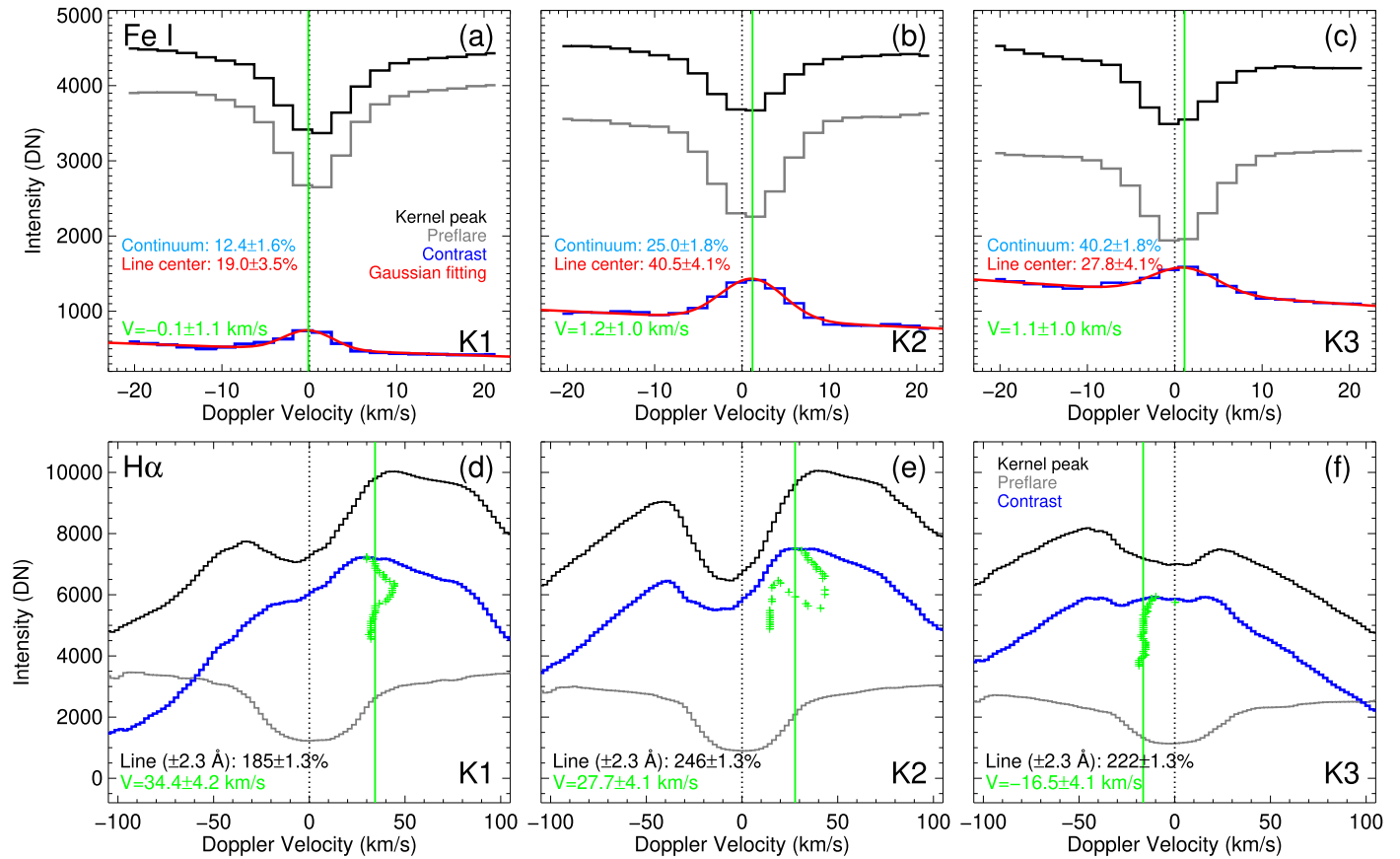
Figure 3. The line profiles of Fe I (a)–(c) and Hα (d)–(f) selected from a single pixel at kernels K1–K3. The gray and black curves refer to the preflare profile and the profile at the peak time, respectively, while the blue curve represents the contrast profile (difference between them). A single Gaussian fitting and a bisector method are used to derive the Doppler velocities for Fe I and Hα, respectively, based on the contrast profiles. The Doppler velocity plus an uncertainty is shown in each panel, together with the relative enhancements of the continuum and Fe I and Hα lines. Note that for Hα, the velocity value represents the median of the velocities at different intensity levels from bisector. The black and green vertical lines in each panel indicate the line center and the median Doppler velocity, respectively.

observations for multiple white-light brightening kernels including K1–K3.

The synthetic Fe I $\lambda6569$ and Hα line profiles for three flare loops (L6, L11, and L4) are shown in Figure 5. The heating episodes of L6 and L11 correspond to the peak times of the white-light emissions from kernels K1 and K2/K3, respectively. Note that the synthetic Fe I $\lambda6173$ profiles look very similar to the ones of Fe I $\lambda6569$ and are not shown here. It is seen that the synthetic Fe I and Hα line profiles are basically similar to the observed ones at K1–K3. The Fe I line shows an absorption profile with the line center enhanced during the heating (Figures 5(a)–(c)). The nearby continuum is also enhanced due to the heating. The Hα line changes from absorption to emission, the latter of which shows a central reversal plus an obvious red asymmetry (Figures 5(d)–(f)). However, it is also seen that the continuum enhancements are only 3.2% and 8.7% for L6 and L11, respectively (Figures 5(a) and (b)), which are much lower than the observed ones of 12.4% and 40.2% at K1 and K3, respectively. Furthermore, the enhancements of Fe I line center for L6 and L11 are 5.4% and 14.2%, respectively, which are also much lower than the observed values of 19.0% and 40.5% at K1 and K2, respectively. Even for L4 with the strongest heating rate and the longest heating time in our simulation (Figure 5(c)), the calculated enhancements are still far from sufficient to explain the observations. Similarly, the synthetic continuum near 6173 Å has a much lower enhancement than the HMI

observations for multiple kernels as well (see Table 1). It should be mentioned that for the Hα line, the simulations can yield a comparable enhancement with the observations for some kernels. The above results reveal that the nonthermal electron-beam heating alone is not enough to produce the white-light enhancements for this flare.

4. Summary and Discussions

In this Letter, we present an X1.0 white-light flare well observed in the Fe I $\lambda6569$ and Hα lines by the recently launched spacecraft CHASE. This flare shows enhancements of ~20% and ~40% at the HMI and CHASE continua, respectively. The CHASE Fe I line is also enhanced up to ~40%. At the white-light kernels, the Fe I line shows a symmetric Gaussian shape with a small redshift of ~1 km s^{-1}. The Hα line changes from absorption to emission with flare heating. The emission profiles display a central reversal and mostly exhibit a red asymmetry with the line center slightly blueshifted. There are also some Hα profiles showing a blue-wing enhancement. The white-light brightenings are cospatial with the microwave footpoint sources and temporally related to the HXR emission above 30 keV. These facts imply that nonthermal electron beams play a role in contributing to the white-light enhancement.

In order to check if the nonthermal electron-beam heating is quantitatively sufficient in producing the white-light emission, we perform observation-constrained radiative hydrodynamic
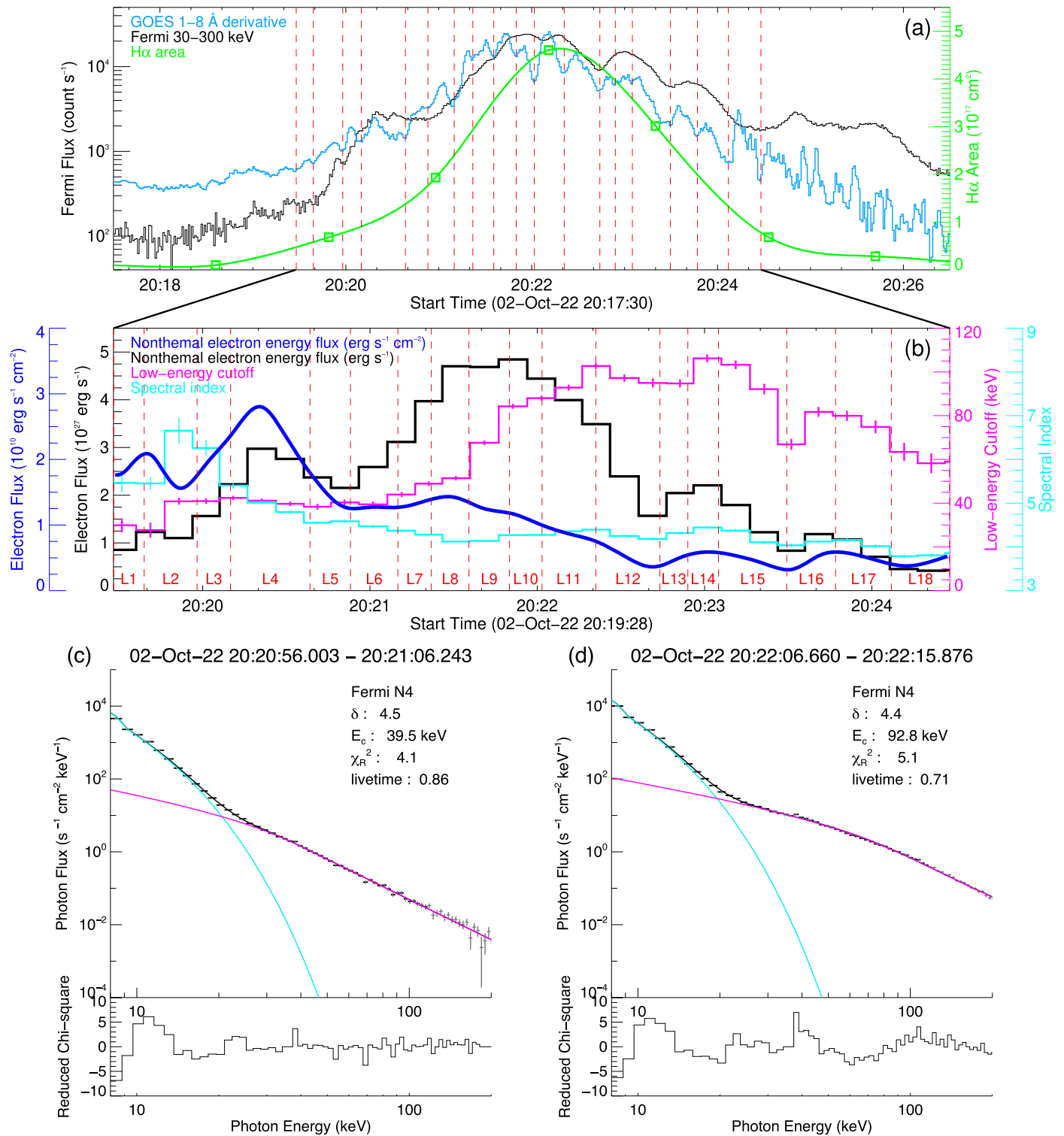
Figure 4. (a) Construction of 18 flare loops based on the GOES SXR 1–8 Å time derivative plus Fermi HXR 30–300 keV emission, with the heating episodes indicated by the red vertical lines. The green curve represents the area of CHASE Hα brightenings after a cubic spline interpolation. (b) Electron-beam parameters including the energy flux, low-energy cutoff, and spectral index used in the simulations for 18 loops (L1–L18). Note that the fitting uncertainties of low-energy cutoff and spectral index are plotted in error bars, which are quite small mostly. (c) and (d) Fermi HXR spectral fitting with a thermal component (cyan) plus a nonthermal component (magenta) for two time intervals corresponding to the heating episodes of L6 (c) and L11 (d) in principle. The fitting parameters including low-energy cutoff (E_c) and spectral index (δ) for the nonthermal component are shown in the panels.

simulations using RADYN. In the simulations, a key parameter is the electron energy flux, which is estimated by the total energy flux divided by the Hα brightening area. Doing so may suffer from a large uncertainty since the area of Hα brightening does not necessarily correspond to the area of electron-beam heating, the latter of which could be much smaller. Therefore, we alternatively use the area of Fe I brightening (about one forth of the Hα area) to obtain a higher energy flux of

Table 1
Electron-beam Parameters in RADYN Simulations and Corresponding Enhancements of the White-light Continua and Fe I Line

Loop	Heating Time (s)	Energy Flux (erg s^{-1} cm^{-2})	Low-energy Cutoff (keV)	Spectral Index	Relative Enhancement (%)					
					RADYN Simulations (VAL-C/penumbral)			HMI & CHASE observations		
					Continuum (near 6173 Å)	Continuum (near 6569 Å)	Line Center (Fe I λ6569)	Continuum (near 6173 Å)	Continuum (near 6569 Å)	Line Center (Fe I λ6569)
L1	11.0	1.9×10^{10}	28.1 ± 3.2	5.4 ± 0.22	1.2/3.2	2.0/5.7	4.0/5.2	...	...	...
L2	19.0	1.6×10^{10}	38.3 ± 1.6	6.4 ± 0.29	2.2/5.3	3.3/8.8	4.9/6.3	...	6.3 ± 1.7 (RoS) 6.5 ± 1.7 (RoS)	9.4 ± 4.1 (RoS) 7.9 ± 4.1 (RoS)
L3	12.0	2.1×10^{10}	41.2 ± 1.3	5.9 ± 0.18	2.2/6.2	3.9/11.3	6.3/9.5	...	...	...
L4	28.5	2.7×10^{10}	40.6 ± 0.9	4.9 ± 0.04	3.1/8.2	4.9/13.5	7.6/13.7	8.2 ± 0.9 (RoS)	...	...
L5	14.5	1.4×10^{10}	39.5 ± 1.4	4.6 ± 0.04	1.8/4.6	2.9/8.0	5.1/9.9	...	...	...
L6	17.0	1.3×10^{10}	39.6 ± 1.3	4.5 ± 0.03	1.9/5.0	3.2/8.8	5.4/8.9	9.8 ± 1.0 (RoS, K1)	12.4 ± 1.6 (RoS, K1)	19.0 ± 3.5 (RoS, K1)
L7	12.0	1.3×10^{10}	47.2 ± 1.1	4.3 ± 0.02	2.0/5.6	3.9/11.2	7.4/12.4	...	...	...
L8	13.5	1.4×10^{10}	50.4 ± 1.0	4.1 ± 0.02	2.4/6.6	4.7/13.2	9.0/15.4	...	...	...
L9	14.5	1.2×10^{10}	72.1 ± 1.1	4.2 ± 0.02	2.9/7.4	5.6/14.5	11.3/18.4	...	...	...
L10	11.7	1.1×10^{10}	87.2 ± 1.1	4.3 ± 0.02	2.1/5.3	4.2/10.8	9.6/17.5	...	...	...
L11	19.3	8.6×10^{9}	93.5 ± 1.3	4.4 ± 0.02	2.3/5.5	3.6/8.7	7.9/14.2	15.3 ± 0.9 (P, K2) 17.6 ± 0.9 (P, K3)	25.0 ± 1.8 (P, K2) 40.2 ± 1.8 (P, K3)	40.5 ± 4.1 (P, K2) 27.8 ± 4.1 (P, K3)
L12	23.0	4.8×10^{9}	96.3 ± 1.7	4.2 ± 0.03	1.2/2.6	1.6/3.5	5.0/9.9	14.5 ± 0.9 (P) 21.0 ± 0.9 (P)	...	...
L13	10.0	4.8×10^{9}	94.0 ± 1.9	4.3 ± 0.03	0.3/1.2	1.1/3.1	4.3/7.6	...	...	...
L14	11.0	5.9×10^{9}	105.9 ± 1.8	4.4 ± 0.04	0.7/2.0	1.6/4.1	5.1/8.8	...	...	...
L15	24.5	4.6×10^{9}	98.3 ± 2.4	4.2 ± 0.04	1.1/2.3	1.5/3.2	4.2/8.1	13.4 ± 0.9 (P) 14.2 ± 0.9 (P)	7.9 ± 1.6 (P) 19.0 ± 1.6 (P)	19.5 ± 3.8 (P) 25.4 ± 3.8 (P)
L16	17.5	4.8×10^{9}	77.7 ± 2.3	4.1 ± 0.04	0.9/2.2	1.8/4.6	5.2/7.4	...	...	...
L17	20.0	5.3×10^{9}	77.3 ± 2.9	4.1 ± 0.04	1.0/2.3	1.6/3.7	4.4/8.4	...	...	...
L18	21.0	4.1×10^{9}	59.4 ± 4.6	3.8 ± 0.05	0.9/2.2	1.8/4.5	4.5/5.9	...	...	...

Note. The nonthermal electron-beam parameters including the energy flux, low-energy cutoff, and spectral index are time dependent. The values here represent those at the middle time of the heating episode for each loop in RADYN simulations. The enhancements of the continua and Fe I line from simulations represent the maximum values in each heating episode. "RoS" and "P" in observations mean that the white-light brightening kernels are located in the region outside the sunspot (corresponding to the VAL-C atmosphere) and in the penumbra, respectively.
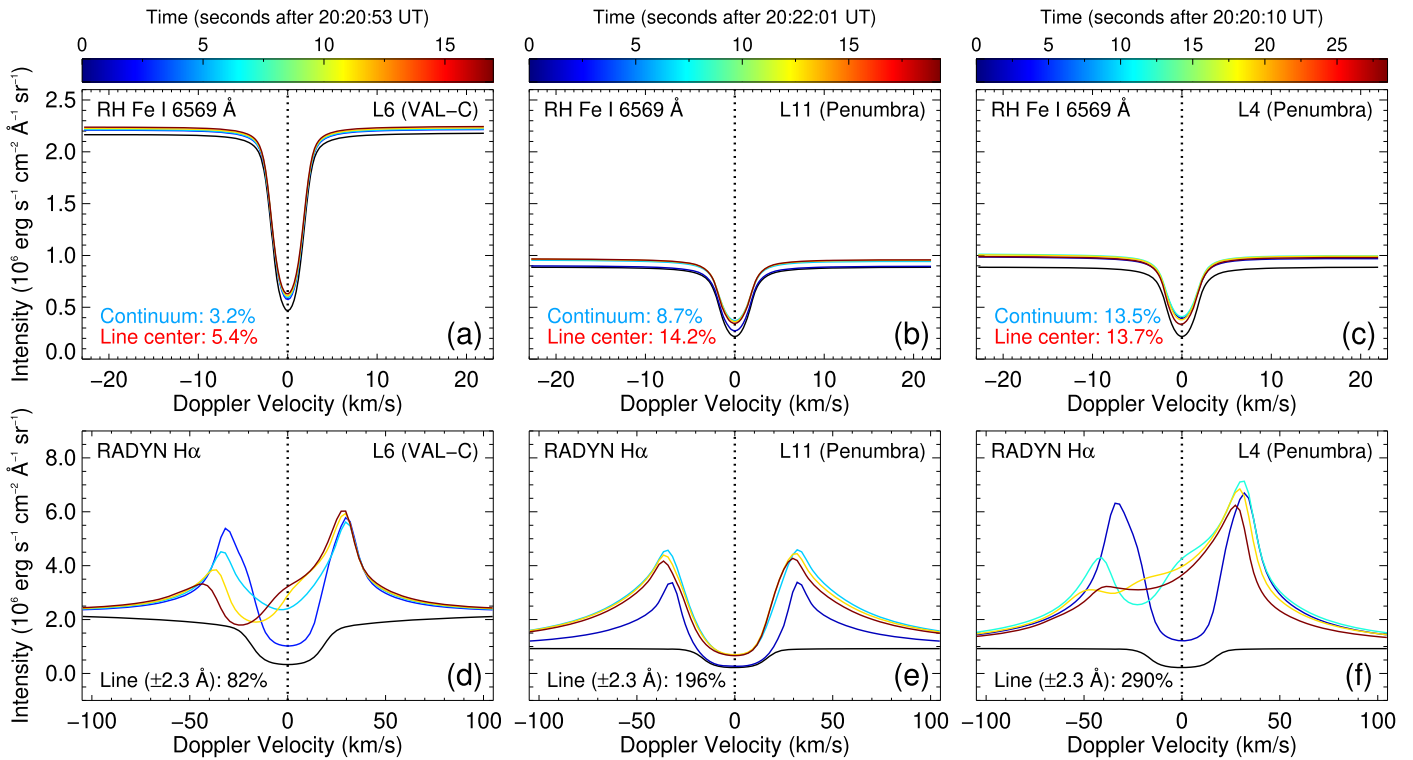
Figure 5. Synthetic Fe I (a)–(c) and Hα (d)–(f) line profiles varying with time for three loops (L6, L11, and L4) in different initial atmospheres. The maximum enhancements of the continuum and Fe I and Hα lines are shown for each loop from the simulations.

3.4×10^{10} erg s^{-1} cm^{-2} in L11. This indeed generates a sufficient enhancement of the Fe I line intensity and nearby continuum. However, this leads to an inconsistency between the calculated Hα line and the observed one, with the former much stronger than the latter, in particular those observed at K2 and K3. If the energy flux becomes greater than 10^{11} erg s^{-1} cm^{-2} (for example, four times the energy flux in L4), the synthetic Fe I profile will change from absorption to emission in the line center, which is obviously inconsistent with the CHASE observations. Another key parameter is the heating time in each loop. If increasing the heating time, we can also obtain a larger enhancement of the continuum and Fe I line. However, a similar problem is that the Hα line would become too strong to match the observed one or that the Fe I line would turn to emission incompatible with the observed line in absorption. In addition to the energy flux and heating time, the low-energy cutoff could bring an uncertainty in the synthetic white-light emission. It is known that the low-energy cutoff determined from spectral fitting is merely an upper limit in the cases where the spectral flattening caused by the cutoff is not clearly seen due to the dominant thermal emission at energies from a few to several tens of keV. This is true for some time intervals in our study (for example, the spectrum shown in Figure 4(c)), which may lead to an underestimation of the total energy flux of nonthermal electron beam. However, as discussed above, increasing the electron energy flux could not well reproduce the observed white-light enhancements or line profiles. In fact, the energy flux carried by the electrons with higher energies (say, ∼50 keV and above) that play a key role in the white-light emission (e.g., Xu et al. 2006; Kuhar et al. 2016) is less affected by the uncertainty of low-energy cutoff. For the spectra with clear spectral flattening (e.g., the spectrum in Figure 4(d)), the cutoff energies are well determined with a

relatively small uncertainty. Note that the obtained low-energy cutoff in a later time (for L9–L18) is above 50 keV, which is significantly larger than the values of 20–40 keV as usually seen in flare studies (e.g., Sui et al. 2005; Aschwanden et al. 2019). However, such high values of low-energy cutoff have also been reported (e.g., Gan et al. 2002; Warmuth et al. 2009; Xia et al. 2021). Actually, the relatively low energy electrons play a minor role (say, the backwarming effect) in generating the white-light emission. On the other hand, the uncertainties of spectral index from the HXR spectral fitting are quite small for this flare as seen in Table 1 and Figure 4(b). Note that although the enhancement of the continuum near Fe I λ6569 may be overestimated in CHASE observations due to the broadening of the nearby Hα line, the continuum near Fe I λ6173 observed by HMI does not suffer from such a problem. According to the above results, we speculate that for this flare, although electron-beam heating is an important source, it is not the sole one. Additional heating sources are required in order to quantitatively produce the observed continuum enhancement as well as the line profile features. Since the RADYN simulations have already included the effects of chromospheric condensation and the radiative backwarming self-consistently, the heating mechanism by Alfvén waves deserves much attention and quantitative studies. It has been suggested that Alfvén waves could deposit the energy in a lower layer such as the temperature minimum region in favor of generating the white-light emission (Emslie & Sturrock 1982; Fletcher & Hudson 2008).

In CHASE observations, the relative enhancement of Fe I line center is greater than that of the nearby continuum for kernels K1 and K2, while the case is reversed for K3. Based on our simulations, the enhanced continuum emission primarily originates from the layers in the middle to lower chromosphere, while the enhanced Fe I line emission mainly comes from the

bottom of the chromosphere. Therefore, the key factor is how deep the electron beam can directly penetrate in the flaring atmosphere, which depends on the preflare atmosphere and the electron-beam parameters as discussed above. Considering that these parameters are quite different in these kernels, it is conceivable that they show different enhancements in the Fe I line and the continuum.

Finally, it is interesting that the observed Hα line profiles show a red (i.e., at K1 and K2) or blue (at K3) asymmetry when the continuum is enhanced. In particular, the asymmetries are opposite for the conjugate footpoints of K2 and K3. The asymmetry of line profiles is usually caused by a plasma flow at the line formation height. For the red asymmetric Hα profiles at K1 and K2, the line center is blueshifted, which could be explained by a chromospheric evaporation flow or an upflow in the formation height of Hα line center (e.g., Kuridze et al. 2015). In the mean time, the Hα line wing could be formed in the chromospheric condensation region with a downflow (e.g., Ding & Fang 1996). As for the blue asymmetry of Hα profiles at K3, one possibility is that the line is still formed in the chromospheric condensation region that causes an absorption at the red wing (Ding & Fang 1996; Kuridze et al. 2015). Another possibility is that the Hα line is formed in a cool upflow layer above the chromospheric evaporation region, which causes a blue-wing enhancement (Tei et al. 2018). As regards the opposite asymmetries of Hα at the conjugate footpoints of K2 and K3, they can be ascribed to different atmospheric conditions as well as different electron-beam heating parameters at the two footpoints.

ORCID iDs

De-Chao Song ⓘ https://orcid.org/0000-0003-0057-6766
Jun Tian ⓘ https://orcid.org/0000-0002-1068-4835
Y. Li ⓘ https://orcid.org/0000-0002-8258-4892
M. D. Ding ⓘ https://orcid.org/0000-0002-4978-4972
Yang Su ⓘ https://orcid.org/0000-0002-4241-9921
Sijie Yu ⓘ https://orcid.org/0000-0003-2872-2614
Jie Hong ⓘ https://orcid.org/0000-0002-8002-7785
Ye Qiu ⓘ https://orcid.org/0000-0002-1190-0173
Shihao Rao ⓘ https://orcid.org/0000-0002-7544-6926
Xiaofeng Liu ⓘ https://orcid.org/0000-0002-3657-3172
Qiao Li ⓘ https://orcid.org/0000-0001-7540-9335
Xingyao Chen ⓘ https://orcid.org/0000-0002-1810-6706
Chuan Li ⓘ https://orcid.org/0000-0001-7693-4908

References

Aschwanden, M. J., Kontar, E. P., & Jeffrey, N. L. S. 2019, ApJ, 881, 1
Babin, A. N., & Koval, A. N. 1992, SvAL, 18, 294
Baranovsky, E. A., & Kurochka, E. V. 1997, A&AT, 13, 173
Brown, J. C. 1971, SoPh, 18, 489
Carlsson, M., & Stein, R. F. 1992, ApJL, 397, L59
Carlsson, M., & Stein, R. F. 2002, ApJ, 572, 626
Carrington, R. C. 1859, MNRAS, 20, 13
Ding, M. D., & Fang, C. 1989, A&A, 225, 204
Ding, M. D., & Fang, C. 1996, SoPh, 166, 437
Ding, M. D., Fang, C., & Yun, H. S. 1999, ApJ, 512, 454
Ding, M. D., Liu, Y., Yeh, C.-T., et al. 2003, A&A, 403, 1151
Emslie, A. G., & Sturrock, P. A. 1982, SoPh, 80, 99
Fang, C., & Ding, M. D. 1995, A&AS, 110, 99
Fang, C., Henoux, J. C., & Gan, W. Q. 1993, A&A, 274, 917
Fletcher, L., & Hudson, H. S. 2008, ApJ, 675, 1645
Gan, W. Q., Li, Y. P., Chang, J., et al. 2002, SoPh, 207, 137
Gan, W. Q., Rieger, E., Zhang, H. Q., et al. 1992, ApJ, 397, 694
Gary, D. E., Chen, B., Dennis, B. R., et al. 2018, ApJ, 863, 83
Hanser, F. A., & Sellers, F. B. 1996, Proc. SPIE, 2812, 344
Hao, Q., Yang, K., Cheng, X., et al. 2017, NatCo, 8, 2202
Henoux, C., & Nakagawa, Y. 1977, A&A, 57, 105
Henoux, J. C., Fang, C., & Gan, W. Q. 1993, A&A, 274, 923
Hiei, E. 1982, SoPh, 80, 113
Hong, J., Ding, M. D., Li, Y., et al. 2018, ApJL, 857, L2
Hong, J., Qiu, Y., Hao, Q., et al. 2022, A&A, 668, A9
Hudson, H. S., Acton, L. W., Hirayama, T., et al. 1992, PASJ, 44, L77
Jurčák, J., Kašparová, J., Švanda, M., et al. 2018, A&A, 620, A183
Kowalski, A. F., Hawley, S. L., Carlsson, M., et al. 2015, SoPh, 290, 3487
Krucker, S., Saint-Hilaire, P., Hudson, H. S., et al. 2015, ApJ, 802, 19
Kuhar, M., Krucker, S., Martínez Oliveros, J. C., et al. 2016, ApJ, 816, 6
Kuridze, D., Mathioudakis, M., Simões, P. J. A., et al. 2015, ApJ, 813, 125
Lemen, J. R., Title, A. M., Akin, D. J., et al. 2012, SoPh, 275, 17
Li, C., Fang, C., Li, Z., et al. 2019, RAA, 19, 165
Li, C., Fang, C., Li, Z., et al. 2022, SCPMA, 65, 289602
Lin, Y., Zhang, H., & Zhang, W. 1996, SoPh, 168, 135
Machado, M. E., Avrett, E. H., Falciani, R., et al. 1986, in The Lower Atmosphere of Solar Flares, 483
Machado, M. E., Emslie, A. G., & Brown, J. C. 1978, SoPh, 58, 363
Martínez Oliveros, J. C., Couvidat, S., Schou, J., et al. 2011, SoPh, 269, 269
Meegan, C., Lichti, G., Bhat, P. N., et al. 2009, ApJ, 702, 791
Metcalf, T. R., Canfield, R. C., Avrett, E. H., et al. 1990, ApJ, 350, 463
Neupert, W. M. 1968, ApJL, 153, L59
Pereira, T. M. D., & Uitenbroek, H. 2015, A&A, 574, A3
Pesnell, W. D., Thompson, B. J., & Chamberlin, P. C. 2012, SoPh, 275, 3
Poland, A. I., Milkey, R. W., & Thompson, W. T. 1988, SoPh, 115, 277
Procházka, O. 2019, Ph.D. Thesis., Queen's Univ. Belfast
Procházka, O., Reid, A., Milligan, R. O., et al. 2018, ApJ, 862, 76
Pugh, C. E., Armstrong, D. J., Nakariakov, V. M., et al. 2016, MNRAS, 459, 3659
Qiu, Y., Rao, S., Li, C., et al. 2022, SCPMA, 65, 289603
Rubio da Costa, F., Kleint, L., Petrosian, V., et al. 2016, ApJ, 827, 38
Scherrer, P. H., Schou, J., Bush, R. I., et al. 2012, SoPh, 275, 207
Song, Y. L., Guo, Y., Tian, H., et al. 2018, ApJ, 854, 64
Sui, L., Holman, G. D., & Dennis, B. R. 2005, ApJ, 626, 1102
Tei, A., Sakaue, T., Okamoto, T. J., et al. 2018, PASJ, 70, 100
Uitenbroek, H. 2001, ApJ, 557, 389
Vernazza, J. E., Avrett, E. H., & Loeser, R. 1981, ApJS, 45, 635
Warmuth, A., Holman, G. D., Dennis, B. R., et al. 2009, ApJ, 699, 917
Watanabe, K., & Imada, S. 2020, ApJ, 891, 88
Xia, F., Su, Y., Wang, W., et al. 2021, ApJ, 908, 111
Xu, Y., Cao, W., Jing, J., et al. 2010, AN, 331, 596
Xu, Y., Cao, W., Liu, C., et al. 2006, ApJ, 641, 1210
Yang, Y.-T., Hong, J., Li, Y., et al. 2021, RAA, 21, 001
Zhou, X., Fang, C., & Hu, J. 1997, ChA&A, 21, 99